Detectability of strongly lensed gravitational waves using model-independent image parameters

Saif Ali,* Evangelos Stoikos,† Evan Meade, Michael Kesden,‡ and Lindsay King§
Department of Physics, The University of Texas at Dallas, Richardson, Texas 75080, USA

(Received 4 October 2022; accepted 19 April 2023; published 12 May 2023)

Strong gravitational lensing of gravitational waves (GWs) occurs when the GWs from a compact binary system travel near a massive object. The lensed waveform is given by the product of the lensing amplification factor F and the unlensed waveform. For many axisymmetric lens models such as the point mass and singular isothermal sphere that we consider, F can be calculated in terms of two lens parameters, the lens mass M_L and source position y. In the geometrical-optics approximation, lensing in these models produces at most two discrete images which can be parametrized by two image parameters, the flux ratio I and time delay Δt_d between images. In the macrolensing regime for which Δt_d is large compared to the time T they spend within the sensitivity band of GW detectors, it is natural to parametrize lensing searches in terms of these image parameters. The functional dependence of the lensed signal on these image parameters is far simpler, facilitating data analysis for events with modest signal-to-noise ratios, and constraints on I and Δt_d can be inverted to constrain M_L and y for any lens model. We propose that this use of image parameters can be extended to the microlensing regime ($\Delta t_d < T$) in which the two interfering images are observed as a single GW event. We use image parameters to determine the detectability of gravitational lensing in GW the microlensing regime and find that for GW events with signal-to-noise ratios ρ and total mass M, lensing should in principle be identifiable for flux ratios $I \gtrsim 2\rho^{-2}$ and time delays $\Delta t_d \gtrsim M^{-1}$.

DOI: 10.1103/PhysRevD.107.103023

I. INTRODUCTION

The first direct detection of gravitational waves (GWs) from merging compact objects was reported by the LIGO and Virgo collaborations in 2016 [1]. To date, Advanced LIGO [2] and Advanced Virgo [3] have reported about 90 events, most of which are mergers between stellar-mass black holes, during their first three observing runs [4]. Kamioka Gravitational Wave Detector (KAGRA) [5–7] has joined the preexisting ground-based GW detectors to form the Advanced LIGO-Virgo-Kagra (LVK) network. The increased sensitivity of detectors such as LVK has allowed us to detect an increasing number of GW events and to perform various general relativistic and cosmological tests [8,9]. With the increasing sensitivity of the current ground-based detector network and future detectors such as the Cosmic Explorer (CE) [10], the Einstein Telescope (ET) [11], the Deci-Hertz Interferometer Gravitational Wave Observatory (DECIGO) [12], and the Laser Interferometer Space Antenna (LISA) [13], the number of observed GW events will increase dramatically, as will the probability of observing new propagation effects such as gravitational lensing that have yet to be detected [14].

When GWs traveling through the Universe encounter a massive object, such as a compact object, galaxy or galaxy cluster, that can act as a lens, deflection of these GWs, i.e. gravitational lensing, will occur [15–21]. Strong lensing of GWs will arise when a lens is very close to the line of sight. In the geometrical-optics approximation, strong lensing will result in the GWs splitting into different lensed images, each with its own magnification and phase [19,22]. There will also be an associated time delay between the lensed images which could range from seconds to years depending on the mass of the lens and geometry of the lens system [23,24].

GW lensing, if detected, could facilitate several exciting scientific studies. It could be used to extract information about the existence of intermediate-mass (mass ranging from $\sim 10^2$–$10^5 M_\odot$) [25] or primordial black holes [26,27] and test general relativity [28–30], including through constraints from GW polarization content [31]. In addition, if a lensed electromagnetic (EM) counterpart of the lensed GW event is observed, it could help to locate the host galaxy at sub-arcsecond precision [32]. Combining the information from the two messengers, i.e. GW and EM lensing, could enable high-precision cosmography [33–38].

There are two major differences between the gravitational lensing of EM waves and GWs from the point of view of wave-optics effects. The first difference is in the applicability of the geometrical-optics approximation. In the case of EM waves, this approximation, typically valid

*sxa180025@utdallas.edu
†Evangelos.Stoikos@utdallas.edu
‡kesden@utdallas.edu
§lindsay.king@utdallas.edu

when the wavelength λ of the waves is much smaller than the Schwarzchild radius R_s of the lens, applies to the vast majority of observations. This is not always the case for GWs, since ground-based detectors such as the LVK network observe at frequencies f in the range 10 Hz $\lesssim f \lesssim 10^4$ Hz, lower than even the lowest-frequency radio telescopes. These GWs have wavelengths longer than the Schwarzschild radii of lenses with masses $M_L \lesssim 10^4 M_\odot$, leading to non-negligible wave-optics effects. The second difference is that the GWs emitted by compact binaries, unlike most EM sources, are coherent, causing interference between lensed images when the signals overlap at the observer.

Lensing in the geometrical-optics approximation can be classified as either macrolensing or microlensing, depending on whether the time delay

$$\Delta t_d \approx M_L = 0.05 \text{ s}\left(\frac{M_L}{10^4 M_\odot}\right), \tag{1}$$

between images is longer or shorter than the time [39]

$$\begin{aligned} T &\approx 5(8\pi f)^{-8/3}\mathcal{M}^{-5/3} \\ &= 1.45 \text{ s}\left(\frac{f}{20 \text{ Hz}}\right)^{-8/3}\left(\frac{\mathcal{M}}{20 M_\odot}\right)^{-5/3} \qquad (2a) \\ &= 33.8 \text{ d}\left(\frac{f}{10^{-4} \text{ Hz}}\right)^{-8/3}\left(\frac{\mathcal{M}}{10^6 M_\odot}\right)^{-5/3}, \qquad (2b) \end{aligned}$$

it takes quasi-circular binaries of chirp mass $\mathcal{M}$ emitting GWs at frequency f to merge. As galaxies have masses $M_L > 10^{10} M_\odot$, they typically generate time delays of hours to days when acting as gravitational lenses. This implies that galactic lenses are deeply in the macrolensing regime for LVK sources with typical parameters $f \gtrsim 20$ Hz and $\mathcal{M} \approx 20 M_\odot$, though not necessarily for LISA sources with typical parameters $f \gtrsim 10^{-4}$ Hz and $\mathcal{M} \approx 10^6 M_\odot$. For LVK sources, the microlensing regime applies to lens masses $M_L \lesssim 10^5 M_\odot$ relevant to intermediate-mass black holes and dark-matter halos too small to host galaxies. In this paper, we focus on the microlensing of LVK sources by such intermediate-mass objects. However, our treatment is also applicable to the microlensing of LISA sources by more massive galactic lenses.

In the frequency domain, the modulation of GWs due to gravitational lensing is characterized by a multiplicative factor known as the amplification factor. In the limit where the geometrical-optics approximation is valid, this factor can be expressed as a sum of terms, each of which corresponds to a discrete image with its own magnification and time delay. For two-image lenses like those considered in this paper, the amplification factor is characterized up to a normalization factor by two image parameters, the flux ratio I and time delay Δt_d between the two images. For a particular axisymmetric lens model, I and Δt_d can be calculated as invertible functions of two lens parameters, the source position y and lens mass M_L [17,19].

In the macrolensing regime, the goal of lensing searches is to determine whether two GW events are really two widely separated images of the same source. It is natural to parametrize such searches [40–42] in terms of the image parameters, as the searches are independent of the underlying lens model. In the microlensing regime, the goal of lensing searches is to distinguish a single lensed GW event from an unlensed event through the modulation induced by the interference between the two simultaneously observed images. A previous study [43] conducted model-dependent microlensing searches in terms of the lens parameters M_L and y. Although this is necessary in the wave-optics regime, we propose that microlensing can still be analyzed in terms of the model-independent image parameters as long as the geometrical-optics approximation is valid. Such model-independent microlensing analyses improve computational efficiency by eliminating the need to iterate through lens models. They also reveal degeneracies between different lens models that give rise to the same image parameters. Using a match-filtering analysis, we explore the mismatch between microlensed and unlensed GW waveforms in both the lens and image parameter spaces and show that this validates our proposal.

This paper is organized as follows. In Sec. II, we begin with a pedagogical outline of gravitational lensing of GWs, discussing the time delay and amplification factor due to the lens. We then present the prescription used to generate the GWs in the inspiral phase of binary compact objects using the post-Newtonian approximation following [39]. In Sec. III, we present a detailed analysis of the point mass (PM) and singular isothermal sphere (SIS) axisymmetric lens-mass profiles and introduce the model-independent image parameters. In Sec. IV, we perform a match-filtering analysis in which we calculate the mismatch between lensed and unlensed GWs. Appendices A and B investigate the mismatch between lensed GW source and unlensed templates. Throughout the paper, we assume $c = G = 1$.

II. BASIC FORMALISM

In this section, we briefly review the basic theory of the gravitational lensing of GWs.

A. Gravitational lensing

In the strong gravitational-lensing regime, we observe multiple images (or a single very distorted image) of a distant background source due to the presence of an intervening massive astrophysical object known as a lens. Lensing occurs when the GWs from a compact binary system travel near a lens as shown for the general lensing geometry in Fig. 1 [24]. The extents of the lens and the source are taken to be much less than the observer-lens and lens-source distances, in which case they can be localized to the lens and source planes. An optic axis connects the observer and the center of the lens. The lens and source

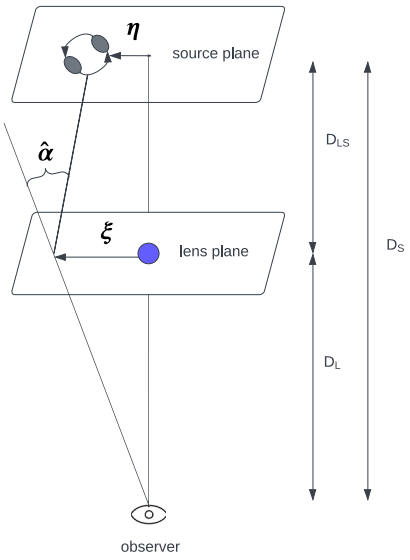

FIG. 1. A typical gravitational lens system consisting of a compact binary system in the source plane, a lens in the lens plane, and an observer. D_L, D_{LS} and D_S are the angular-diameter distances from observer to lens, lens to source, and observer to source respectively. The vector $\boldsymbol{\xi}$ is the impact parameter in the lens plane, and the vector $\boldsymbol{\eta}$ is the location of the source with respect to the optic axis in the source plane. $\hat{\boldsymbol{\alpha}}$ is the deflection angle measured on the lens plane.

planes are at angular-diameter distances D_L and D_S respectively. The angular-diameter distance between the lens and source planes is D_{LS}. A GW source is located on the source plane at displacement $\boldsymbol{\eta}$ with respect to the optic axis. After being emitted by the source, the GWs travel to the lens plane, with an impact parameter $\boldsymbol{\xi}$, and are deflected through an angle $\hat{\boldsymbol{\alpha}}$ by the gravitational potential of the lens. $\mathbf{x} \equiv \boldsymbol{\xi}/\xi_0$ and $\mathbf{y} \equiv \boldsymbol{\eta}/(\xi_0 D_S/D_L)$ are dimensionless vectors on the lens and source plane respectively, where ξ_0 is a model-dependent characteristic length scale on the lens plane called the Einstein radius. GWs that reach the observer satisfy the lens equation

$$\mathbf{y} = \mathbf{x} - \boldsymbol{\alpha}(\mathbf{x}), \tag{3}$$

where

$$\boldsymbol{\alpha}(\mathbf{x}) = \frac{D_L D_{LS}}{\xi_0 D_S}\hat{\boldsymbol{\alpha}}(\xi_0 \mathbf{x}) = \nabla_x \psi(\mathbf{x}), \tag{4}$$

is the scaled deflection angle at the observer. The lensing potential $\psi(\mathbf{x})$ is given by the two-dimensional Poisson equation

$$\nabla_x^2 \psi(\mathbf{x}) = \frac{2\Sigma(\mathbf{x})}{\Sigma_{\rm cr}}, \tag{5}$$

where Σ is the surface mass density of the lens and $\Sigma_{\rm cr} \equiv D_S/4\pi D_L D_{LS}$ is the critical surface mass density. For the formation of multiple images, $\Sigma/\Sigma_{\rm cr} > 1$ is a sufficient, but not necessary condition [44].

Gravitational lensing causes a time delay between the lensed images at the observer. The arrival time has two components, one arising from the geometry of the path traveled, and the other due to the gravitational potential of the lens known as the Shapiro time delay. The time delay at the observer due to a lens at redshift z_L is

$$t_d(\mathbf{x},\mathbf{y}) = \frac{D_S \xi_0^2 (1+z_L)}{D_L D_{LS}}\left[\frac{1}{2}|\mathbf{x}-\mathbf{y}|^2 - \psi(\mathbf{x}) + \phi_m(\mathbf{y})\right], \tag{6}$$

where $\phi_m(\mathbf{y})$ is chosen such that the minimum value of the time delay is 0.

The lensing amplification factor $F(f) = \tilde{h}^L(f)/\tilde{h}(f)$ relates the lensed waveform $\tilde{h}^L(f)$ to the unlensed waveform $\tilde{h}(f)$ for GWs of frequency f. It is given by Kirchhoff's diffraction integral [19,24]

$$F(f) = \frac{D_S \xi_0^2 (1+z_L)}{D_L D_{LS}}\frac{f}{i}\int d^2\mathbf{x}\, \exp[2\pi i f t_d(\boldsymbol{x},\boldsymbol{y})]. \tag{7}$$

This integral over the lens plane accounts for all the trajectories in which the wave can propagate; it is unity in the absence of a lens.

1. Geometrical-optics approximation

In the geometrical-optics approximation, generally valid for GW frequencies f and lens masses M_L for which $f \gg M_L^{-1}$ [45], discrete images form at the stationary points $\mathbf{x}_j$ of the time-delay function at which $\nabla_x t_d(\mathbf{x},\mathbf{y}) = 0$. Only these points contribute to the lensing amplification factor

$$F(f) = \sum_j |\mu_j|^{1/2} \exp(2\pi i f t_d(\mathbf{x}_j,\mathbf{y}) - i\pi n_j), \tag{8}$$

where $\mu_j = 1/\det(\partial \mathbf{y}/\partial \mathbf{x}_j)$ is the magnification of the jth image and the Morse index n_j has values of 0, 1/2, or 1 depending on whether $\mathbf{x}_j$ is a minimum, saddle point, or maximum respectively of the time-delay surface, $t_d(\mathbf{x},\mathbf{y})$.

B. Gravitational waveform

We restrict our analysis to the inspiral phase of the GW evolution from binary black hole (BBH) mergers and use the post-Newtonian (PN) approximation to model our unlensed waveform [39]

$$\tilde{h}(f) = \begin{cases} \frac{A}{D}\mathcal{M}^{5/6} f^{-7/6} e^{i\Psi(f)}, & 0 < f < f_{\rm cut} \\ 0, & f_{\rm cut} < f, \end{cases} \tag{9}$$

where D is the luminosity distance to the source, $\Psi(f)$ is the GW phase, and the GW amplitude A is a function of sky localization and source geometry of order unity as discussed in [46]. For a BBH system with masses m_1 and m_2, $M = m_1 + m_2$ is the total mass, $\eta = m_1 m_2/M^2$ is the symmetric mass ratio, $M_z = (1+z)M$ is the redshifted total mass, and $\mathcal{M} = \eta^{3/5} M_z$ is the redshifted chirp mass.

The cutoff frequency $f_{\rm cut} = 1/(6^{3/2}\pi M_z)$ is chosen to be twice the orbital frequency at the innermost stable circular orbit of a BH of mass M_z.

To 1.5PN order [39], the GW phase is

$$\Psi(f) = 2\pi f t_c - \phi_c - \frac{\pi}{4} + \frac{3}{4}(8\pi\mathcal{M}f)^{-\frac{5}{3}}\left[1 + \frac{20}{9}\left(\frac{743}{336} + \frac{11\eta}{4}\right)x - 16\pi x^{\frac{3}{2}}\right], \tag{10}$$

where t_c and ϕ_c are the coalescence time and phase and $x \equiv (\pi M_z f)^{2/3}$ is the PN expansion parameter.

Our restriction to the inspiral stage of waveforms is a reasonable approximation for this study of microlensing, as the interference between the two images can most readily be observed as the binaries inspiral through a frequency range $\Delta f \gtrsim \Delta t_d^{-1}$. Although the merger and ringdown stages can make significant contributions to the total signal-to-noise ratio (SNR), they occur over a narrow range in frequencies making the effects of microlensing degenerate with changes to the luminosity distance D and coalescence phase ϕ_c.

III. AXISYMMETRIC LENS MODELS

In this section, we discuss two axisymmetric lens models, the singular isothermal sphere (SIS) and the point mass (PM), that produce at most two images in the geometrical-optics approximation. We introduce model-independent image parameters that describe the amplification factor F in this approximation, and assess the validity of these new parameters as the geometrical-optics approximation breaks down at low frequencies.

A. Singular isothermal sphere (SIS)

The SIS density profile $\Sigma(\boldsymbol{\xi}) = \sigma_v^2/2\xi$, where σ_v is the velocity dispersion, is the most simple profile that can effectively describe the flat rotation curves of galaxies [47]. It leads to the lensing potential $\psi(x) = x$ by Eq. (5) and the amplification factor [19,48]

$$\begin{aligned} F(f) &= -iwe^{iwy^2/2}\int_0^\infty dx\, xJ_0(wxy) \\ &\quad\times \exp\left[iw\left(\frac{1}{2}x^2 - x + \phi_m(y)\right)\right] \\ &= e^{\frac{i}{2}w(y^2+2\phi_m(y))}\sum_{n=0}^{\infty}\frac{\Gamma(1+\frac{n}{2})}{n!} \\ &\quad\times (2we^{i\frac{3\pi}{2}})^{\frac{n}{2}}{}_1F_1\left(1+\frac{n}{2},1;-\frac{i}{2}wy^2\right), \end{aligned} \tag{11}$$

by Eq. (7), where $w = 8\pi M_L f$, $\phi_m(y) = y + 1/2$, J_0 is the Bessel function of zeroth order, $\xi_0 = 4\pi\sigma_v^2 D_L D_{LS}/D_S$ is the Einstein radius, and $M_L = \pi\sigma_v^2(1+z_L)\xi_0$ is the lens mass inside the Einstein radius.

B. Point mass (PM)

The PM is the simplest mass distribution for a gravitational lens. It leads to a lensing potential $\psi(x) = \ln x$ and amplification factor [19,49]

$$\begin{aligned} F(f) &= \exp\left\{\frac{\pi w}{4} + i\frac{w}{2}\left[\ln\left(\frac{w}{2}\right) - 2\phi_m(y)\right]\right\} \\ &\quad\times\Gamma\left(1-\frac{i}{2}w\right){}_1F_1\left(\frac{i}{2}w,1;\frac{i}{2}wy^2\right), \end{aligned} \tag{12}$$

where $w = 8\pi M_L f$, $\phi_m(y) = (x_m - y)^2/2 - \ln x_m$, $x_m = (y + (y^2+4)^{1/2})/2$, and ${}_1F_1(a,b;c)$ is the confluent hypergeometric function. The Einstein radius ξ_0 for a PM of lens mass M_L is $\xi_0 = [4M_L D_L D_{LS}/D_S(1+z_L)]^{1/2}$.

C. Geometrical-optics approximation

In the limit where the geometrical-optics approximation is valid, a source at position $\mathbf{y}$ creates a discrete number of images at positions $\mathbf{x}_j$ which are stationary points of the time delay $t_d(\mathbf{x},\mathbf{y})$ given by Eq. (6). For the SIS lens, only one image is formed if the source is outside the unit circle ($y > 1$), whereas two images are formed if the source is inside ($y < 1$). The amplification factor $F(f)$ in the geometrical-optics approximation of Eq. (8) is given by [19]

$$F(f) = \begin{cases} |\mu_+|^{1/2} - i|\mu_-|^{1/2}e^{2\pi i f\Delta t_d}, & y < 1 \\ |\mu_+|^{1/2}, & y > 1, \end{cases} \tag{13}$$

where

$$\mu_\pm = \pm 1 + \frac{1}{y}, \tag{14a}$$

$$\Delta t_d = 8M_L y. \tag{14b}$$

As a PM lens can deflect photons by an arbitrarily large angle for sufficiently small impact parameter, there are two images for all source positions y. $F(f)$ is given by [19]

$$F(f) = |\mu_+|^{1/2} - i|\mu_-|^{1/2}e^{2\pi i f\Delta t_d}, \tag{15}$$

where

$$\mu_\pm = \frac{1}{2} \pm \frac{y^2+2}{2y(y^2+4)^{1/2}}, \tag{16a}$$

$$\Delta t_d = 2M_L\left\{y(y^2+4)^{1/2} + 2\ln\left[\frac{(y^2+4)^{1/2}+y)}{(y^2+4)^{1/2}-y)}\right]\right\}. \tag{16b}$$

Both the SIS and PM lens models can be parametrized by two lens parameters, the source position y and lens mass M_L.

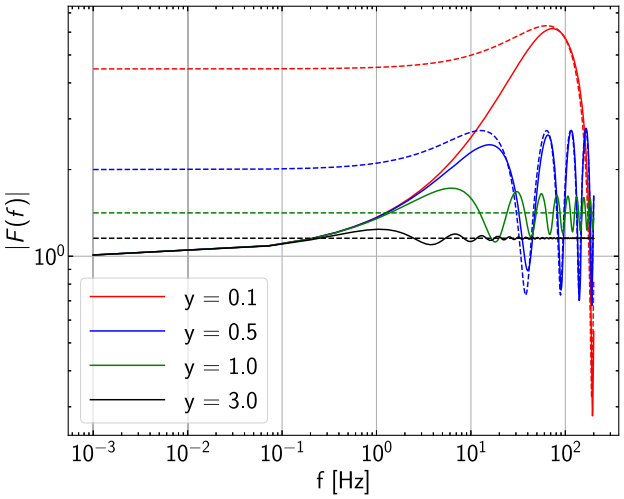

FIG. 2. The magnitude of the amplification factor $F(f)$ as a function of frequency f for an SIS with lens mass $M_L = 10^3 M_\odot$ and source positions $y = 0.1$, 0.5, 1.0, and 3.0 shown in red, blue, green, and black. The solid lines are calculated using the exact result of Eq. (11), while the dashed lines are calculated using the geometrical-optics approximation of Eq. (13).

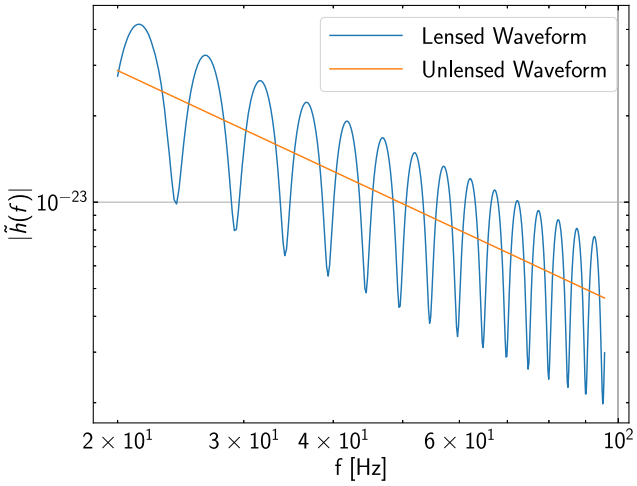

FIG. 3. Waveform magnitudes as functions of frequency f for our default source parameters of $A = 0.21$, $\mathcal{M} = 20M_\odot$, $\eta = 0.25$, $t_c = \phi_c = 0$, and $D = 1$ Gpc. The orange line shows the unlensed waveform $\tilde{h}(f)$, while the blue curve shows the lensed waveform $\tilde{h}^L(f) = F(f)\tilde{h}(f)$ for the amplification factor $F(f)$ of a SIS with lens parameters $y = 0.5$ and $M_L = 10^4 M_\odot$ calculated in the geometrical-optics approximation.

The amplification factor $F(f)$ for the SIS is shown in Fig. 2. In the low-frequency limit, $F(f)$ converges to unity because diffraction effects prevent long-wavelength GWs from being affected by the presence of a lens [19,50]. In the high-frequency limit, the geometrical-optics approximation is valid and oscillatory behavior is observed due to interference between the coherent lensed images. We assume that the time delay Δt_d is much less than the observing time of the GW detector as is appropriate for the lens mass shown in Fig. 2.

Figure 3 shows the unlensed waveform $\tilde{h}(f)$ and lensed waveform $\tilde{h}^L(f) = F(f)\tilde{h}(f)$ as functions of frequency f. The unlensed waveform given by Eq. (9) is parametrized by the GW amplitude A, redshifted chirp mass $\mathcal{M}$, symmetric mass ratio η, source luminosity distance D, coalescence time t_c, and coalescence phase ϕ_c; we choose fiducial values of $A = 0.21$, $\mathcal{M} = 20M_\odot$, $\eta = 0.25$, $t_c = \phi_c = 0$, and $D = 1$ Gpc for these source parameters. It is proportional to $f^{-7/6}$ according to Eq. (9) and appears as a straight line in this log-log plot. The lensed waveform is calculated for a SIS with lens parameters $y = 0.5$ and $M_L = 10^4 M_\odot$ and displays oscillatory behavior due to interference between the two terms in Eq. (13).

D. Model-independent image parameters

When the amplification factor $F(f)$ is given by Eq. (15), i.e. the source position is such that two images are formed and the geometrical-optics approximation is valid, we can express this factor directly in terms of the flux ratio $I = |\mu_-|/|\mu_+|$ and time delay Δt_d between the images. These "image parameters" are model-independent in that they fully specify the amplification factor for any two-image lens model up to an overall normalization that is observationally degenerate with the GW amplitude A. The relationship between these image parameters and lens parameters like the source position y and lens mass M_L is model dependent; these relations for the SIS and PM lens models are given by Eqs. (14) and (16) respectively.

In Fig. 4, we plot the flux ratio I and time delay Δt_d as parametric functions of the source position y for our two

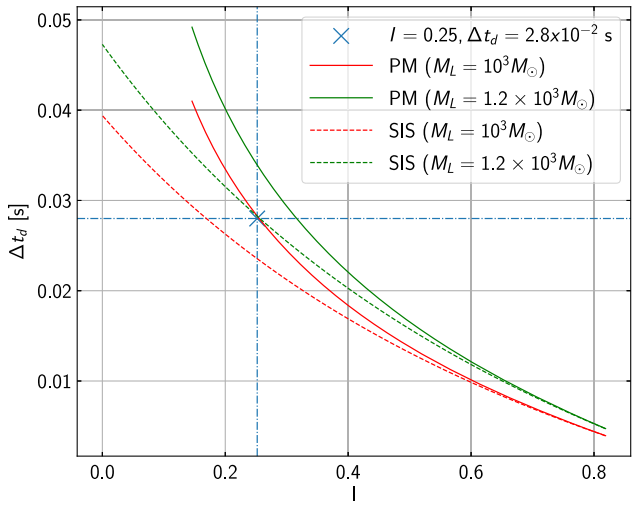

FIG. 4. The flux ratio I and time delay Δt_d as parametric functions of the source position y for two-image lens models of varying lens mass M_L. The solid (dashed) curves correspond to the PM (SIS) lens model, while the red (green) curves are for a lens mass $M_L = 10^3 M_\odot$ ($1.2 \times 10^3 M_\odot$). The blue cross indicates the point ($I = 0.25$, $\Delta t_d = 2.8 \times 10^{-2}$ s) where curves for the PM and SIS models intersect.

axisymmetric lens models and two choices of the lens mass M_L. The blue cross indicates specific, potentially observable values ($I = 0.25$ and $\Delta t_d = 2.8 \times 10^{-2}$ s) of the model-independent image parameters. According to Eqs. (14) and (16), these values can be obtained in both the SIS and PM lens models, albeit with different lens parameters, $M_L \approx 1.2 \times 10^3 M_\odot$ and $y \approx 0.6$ for the SIS lens and $M_L \approx 10^3 M_\odot$ and $y \approx 0.7$ for the PM lens. This analysis reveals that apart from any observational errors associated with measuring the image parameters I and Δt_d, there is a $\sim 20\%$ model dependence with which lens parameters like M_L and y can be reconstructed.

To further illustrate that the same image parameters can be produced by different choices of lens parameters in different lens models, in Fig. 5 we show the ratio of the lens mass $M_L^{\rm PM}$ in the PM model to the lens mass $M_L^{\rm SIS}$ in the SIS model that produce the same flux ratio $I \equiv |\mu_-|/|\mu_+|$ and time delay Δt_d. To obtain this ratio, we invert Eqs. (14a) and (16a) to obtain the source distances $y^{\rm SIS}$ and $y^{\rm PM}$ in the SIS and PM models, respectively. We then equate Eqs. (14b) and (16b) and insert these source distances to obtain the ratio $M_L^{\rm PM}/M_L^{\rm SIS}$. The fact that this ratio is less than unity could be interpreted as indicated that the more compact PM model is a more powerful lens than the SIS model; it can produce the same image parameters at a smaller lens mass. The difference between this mass ratio and unity provides a lower bound on the systematic fractional uncertainty with which the lens mass can be measured in microlensing events due to model uncertainty, even if the image parameters were measured with arbitrary precision.

A recent study [43] investigated whether a GW150914-like GW event microlensed by a point mass with $M_L^{PM} = 10^3 M_\odot$ and source position $y^{\rm PM} = 1$ could be distinguished from lensing by a SIS lens model. Parameter estimation was performed for this event in both the correct PM and incorrect SIS models. The input parameters were accurately recovered in the PM model, but in the SIS model the best-fit parameters were $M_L^{\rm SIS} = 1468 M_\odot$ and $y^{\rm SIS} = 0.72$. Assuming that the geometrical-optics approximation held for this event, we would predict image parameters

$$I = \frac{|\mu_-^{\rm PM}|}{|\mu_+^{\rm PM}|} = \frac{3-\sqrt{5}}{3+\sqrt{5}} = 0.146 \tag{17a}$$

$$\Delta t_d = 2M_L\left[\sqrt{5} + 2\ln\left(\frac{\sqrt{5}+1}{\sqrt{5}-1}\right)\right] = 41.6 \text{ ms}, \tag{17b}$$

for this event. A SIS model with lens parameters

$$y^{\rm SIS} = \frac{1-I}{1+I} = 0.745 \tag{18a}$$

$$M_L^{\rm SIS} = \frac{\Delta t_d}{8 y^{\rm SIS}} = 1396 M_\odot, \tag{18b}$$

would yield the same image parameters. We see that these estimates are very close to the best-fit parameters in the SIS model, despite the fact that $w = 8\pi M_L f = 0.25$ is not that large at the bottom of the LVK sensitivity band at $f = 20$ Hz, suggesting that wave-optics effects may be significant. The validity of these estimates supports our contention that the use of image parameters is still valuable in the microlensing regime despite the absence of two widely separated images.

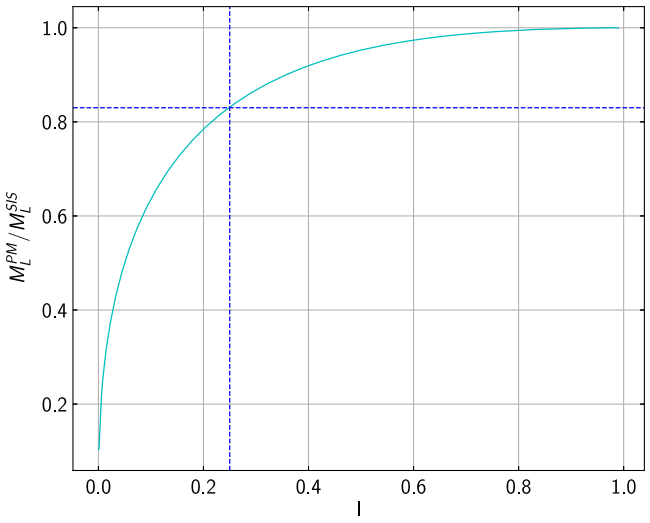

FIG. 5. The mass ratio $M_L^{\rm PM}/M_L^{\rm SIS}$ of point-mass (PM) to singular-isothermal-sphere (SIS) models producing the same flux ratio I for equal time delay Δt_d. The vertical blue dashed line corresponds to $I = 0.25$ like the vertical blue dot-dashed line in Fig. 4.

IV. MATCHED-FILTERING ANALYSIS

In this section, we perform a matched-filtering analysis to quantify the difference between lensed and unlensed GWs. The mismatch ϵ between two waveforms h_1 and h_2 is defined as [39]

$$\epsilon(h_1, h_2) \equiv 1 - \max_{t_c, \phi_c} \frac{\langle h_1|h_2\rangle}{\sqrt{\langle h_1|h_1\rangle\langle h_2|h_2\rangle}}. \tag{19}$$

The noise-weighted inner product $\langle h_1|h_2\rangle$ between the waveforms h_1 and h_2 is defined as

$$\langle h_1|h_2\rangle = 4\text{Re}\int_{f_{\rm low}}^{f_{\rm cut}} df \frac{h_1(f)h_2^*(f)}{S_n(f)}, \tag{20}$$

where $S_n(f)$ is the noise power spectral density (PSD). We use the PYCBC.FILTER package [51] to evaluate the mismatch between waveforms. The two waveforms h_1 and h_2 can be distinguished when their mismatch $\epsilon \gtrsim \rho^{-2}$, where $\rho = \langle h|h\rangle^{1/2}$ is the SNR of a waveform h [39,52,53].

Figure 6 shows contour plots of the mismatch ϵ between lensed GW source and unlensed templates as functions of the model-dependent lens parameters y and M_L (left panels) and the model-independent image parameters I and Δt_d (right

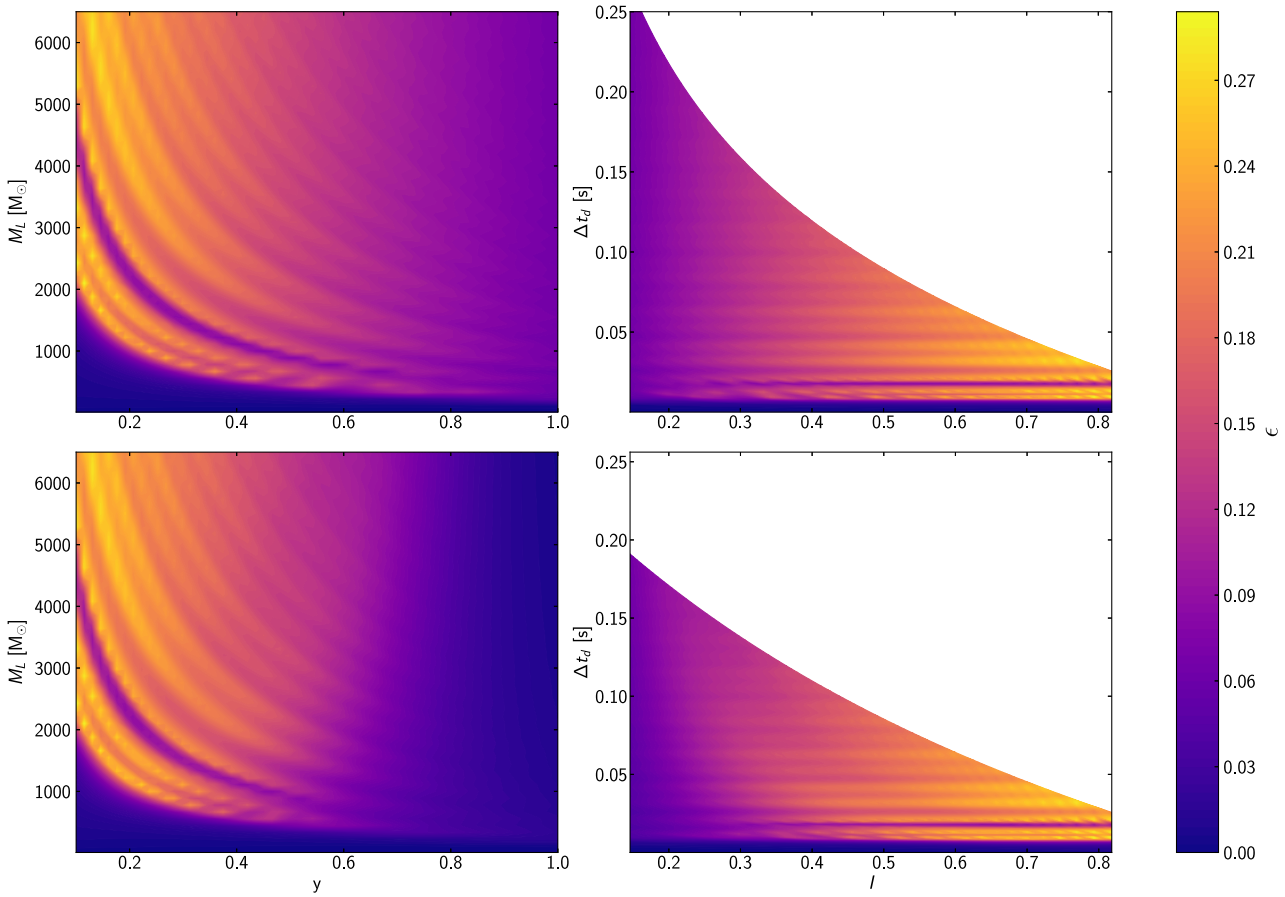

FIG. 6. Contour plots of the mismatch ϵ between lensed and unlensed GWs for PM lenses (top panels) and SIS lenses (bottom panels). The left panels show ϵ as a function of the model-dependent source distance y and lens mass M_L, while the right panels show ϵ as a function of the model-independent flux ratio I and time delay Δt_d. The unlensed waveforms are calculated using the default source parameters $\mathcal{M} = 20M_\odot$, $\eta = 0.25$, and $t_c = \phi_c = 0$.

panels) for PM lenses (top panels) and SIS lenses (bottom panels). We use the same source parameters for the lensed and unlensed templates and the noise PSD appropriate for a single two-armed detector with aLIGO design sensitivity. The mismatches as functions of the lens parameters are qualitatively similar for the PM (top left panel) and SIS (bottom left panel) models. For a vanishing lens mass ($M_L \to 0$), diffraction causes the amplification factor to approach unity ($F \to 1$) and the mismatch to vanish ($\epsilon \to 0$) according to Eq. (19) for $h_1 = h_2$. The biggest difference between the two models occurs in the limit $y \to 1$, where $|\mu_-| \to 0$ for the SIS model according to Eq. (14a) but $|\mu_-| \to 0.17$ for the PM model according to Eq. (16a). This accounts for the much smaller mismatches for the SIS model compared to the PM model in this limit.

The PM and SIS models become qualitatively indistinguishable when the mismatch is expressed as a function of the image parameters of I and Δt_d as shown in the right panels of Fig. 6. Although the top and bottom panels appear the same in the regions where they overlap, the PM model extends to larger values of the time delay Δt_d than the SIS model at small flux ratios I. This occurs because the mappings Eqs. (14) and (16) between the lens parameter space in the left panels and the image parameter space in the right panels are model-dependent.

The better agreement between the mismatches in the PM and SIS lens models when expressed as functions of the image parameters I and Δt_d can be seen even more clearly in Fig. 7. This figure shows the difference $\Delta\epsilon = |\epsilon_{\rm PM} - \epsilon_{\rm SIS}|$ between the mismatches for PM and SIS lens models shown in the top and bottom panels of Fig. 6. The left panel of Fig. 7 shows large differences $\Delta\epsilon \gtrsim 0.15$ between the two lens models for source distances $y \gtrsim 0.7$ where the flux ratio I vanishes in the SIS model but not the PM model. However, when the mismatch difference is expressed as a function of the image parameters in the right panel, the amplification factors and thus the mismatches only have significant differences for $\Delta t_d \lesssim 0.02$ s where the geometrical-optics approximation breaks down.

The right panels of Fig. 6 also reveal that the crests and troughs of the oscillations in ϵ occur on lines of constant time delay Δt_d. We examine these oscillations and the general dependence of the mismatch on our lens and image parameters for the SIS model in Fig. 8. The top left (right)

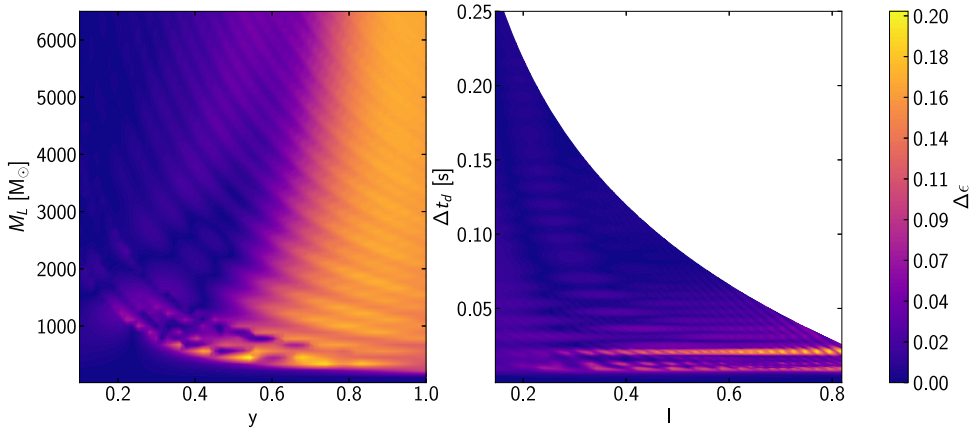

FIG. 7. The difference $\Delta\epsilon = |\epsilon_{\rm PM} - \epsilon_{\rm SIS}|$ between the mismatches between lensed and unlensed waveforms for PM and SIS lens models shown in the top and bottom panels of Fig. 6 as functions of the source position y and lens mass M_L (left panel) and the flux ratio I and time delay Δt_d (right panel).

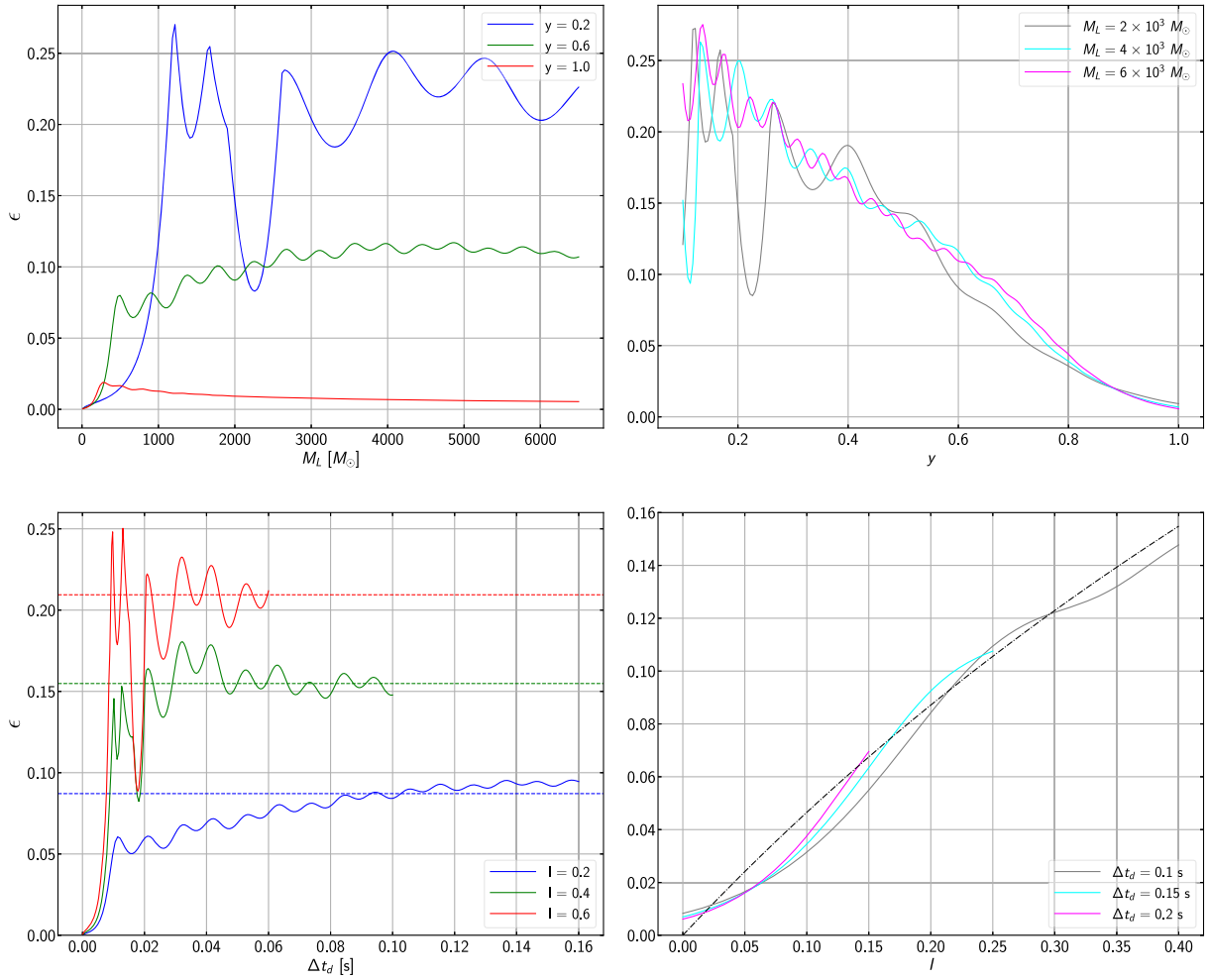

FIG. 8. The mismatch ϵ between lensed and unlensed waveforms with source parameters $\mathcal{M} = 20M_\odot$, $\eta = 0.25$, and $t_c = \phi_c = 0$ in the SIS lens model as a function of lens mass M_L (top left panel), source position y (top right panel), time delay Δt_d (bottom left panel), and flux ratio I (bottom right panel). In the top (bottom) left panel, the blue, green, and red curves correspond to $y = 0.2$, 0.6, and 1.0 ($I = 0.2$, 0.4, and 0.6). In the top (bottom) right panel, the gray, cyan, and magenta curves correspond to $M_L = 2 \times 10^3 M_\odot$, $4 \times 10^3 M_\odot$, and $6 \times 10^3 M_\odot$ ($\Delta t_d = 0.1$ s, 0.15 s, and 0.2 s). The dotted curves in the bottom panels show the mismatch $\epsilon \approx 1 - (1 + I)^{-1/2}$ in the extreme geometrical-optics limit derived in Appendix A.

panels of Fig. 8 show vertical (horizontal) slices of the bottom left panel of Fig. 6 along lines of constant y (M_L). The dependence of the mismatch ϵ on these lens parameters is non-monotonic and difficult to interpret, exhibiting oscillations of varying amplitude, frequency, and phase and a deep valley. The dependence of ϵ on the image parameters Δt_d and I shown in the bottom panels is far easier to interpret. The bottom left panel shows that $\epsilon \to 0$ in the diffraction limit $\Delta t_d \to 0$, while in the opposite extreme geometrical-optics limit $\Delta t_d \to \infty$, $\epsilon \to 1-(1+I)^{-1/2}$ as derived in Appendix A. The crests and troughs of the oscillations, as well as the deep valley at $\Delta t_d \approx 0.015$ s are all aligned in this panel, reinforcing our contention that these oscillations are purely functions of the time delay Δt_d. They are absent in the bottom right panel, where Δt_d is held constant and the mismatch depends smoothly on the flux ratio I in reasonable agreement with the extreme geometrical-optics limit $\epsilon \to 1-(1+I)^{-1/2}$.

We investigate the oscillations in the mismatch ϵ as a function of the time delay Δt_d in Appendix B. These oscillations result from the number and location of the peaks of the amplification factor $F(f)$ shown in Fig. 2 within the sensitivity band of the detector changing as Δt_d varies. For our approximate waveform of Eq. (9), the sharpest feature in the detector response is a cutoff in the strain $h(f)$ above a frequency $f_{\rm cut} = (6^{3/2}\pi M_z)^{-1}$. According to Eq. (B3), this cutoff couples to the peaks of the amplification factor to create oscillations in the mismatch with frequency as a function of the time delay with frequency $f_{\rm cut}$ and amplitude proportional to $I^{3/2}/(1+I)$. Numerical-relativity simulations reveal that true waveforms transition smoothly to a ringdown rather than experiencing such a sharp cutoff [54–56], but the merger should still imprint a feature leading to oscillations in the mismatch between a lensed GW source and unlensed templates. Our analysis suggests that these oscillations may be significant for large flux ratios I (small source distances y), implying that serendipity between the lens parameters and source mass may facilitate the discovery of lensing in GW events.

V. DISCUSSION

In the geometrical-optics approximation, strong gravitational lensing produces multiple images. The lensing amplification factor $F(f)$ can be expressed as a summation over these images, each with its own magnification μ_j, time delay $t_{d,j}$, and Morse index n_j as given by Eq. (8). In any given lens model, these image parameters can be calculated as functions of the lens parameters such as the source position $\mathbf{y}$ and the lens mass M_L. Lensing of transient events can further be classified as either microlensing or macrolensing, depending on whether the time delay between images is shorter or longer than the duration of the transient. In the latter case, two distinct GW events are observed and it is natural to characterize these events using image parameters. We propose that, even in the microlensing regime, observational searches for strong lensing in GW events, as well as theoretical studies of their feasibility, should be conducted in terms of these model-independent image parameters rather than the model-dependent lens parameters provided that the geomertrical-optics approximation still holds.

In this paper, we investigate this proposal by considering two well-known axisymmetric lens models: the singular isothermal sphere (SIS) and the point mass (PM). The SIS model has a density profile $\rho \propto r^{-2}$ appropriate for a galaxy or stellar cluster, while the PM model could describe an individual star or compact object. In the geometrical-optics approximation, the SIS produces two images for source positions $y < 1$, while the PM always produces two images. For the case of two images, the amplification factor is given by Eq. (15) for both models, but the mappings between the image parameters (the flux ratio $I = |\mu_-|/|\mu_+|$ and the time delay Δt_d) and the lens parameters (the source distance y and the lens mass M_L) are model dependent and given by Eqs. (14) and (16) respectively. This implies that uncertainty in the lens model will translate into uncertainty in the lens parameters, even if the image parameters could be measured with arbitrary precision. We illustrate this in Fig. 4, where the SIS and PM models can generate images with identical flux ratios and time delays despite have lens parameters that differ by $\sim 20\%$. This represents a conservative estimate of the systematic error in the lens parameters associated with uncertainty in the lens model, as the PM model is more compact than any real galaxy or halo. Figure 5 reveals that this systematic error gets even larger as the flux ratio decreases.

Lensed GW events with finite signal-to-noise ratios ρ can be distinguished from unlensed templates if the minimum mismatch ϵ between the lensed signal and members of the template bank exceeds ρ^{-2} [39,52,53]. The oscillatory features induced in the waveform by lensing in the geometrical-optics limit depicted in Fig. 3 have little degeneracy with the source parameters specifying the unlensed waveform in Eqs. (9) and (10), so we approximate this minimum mismatch by that between lensed and unlensed waveforms with the same source parameters. In this approximation, the mismatch can be approximated by $\epsilon \approx 1-(1+I)^{-1/2}$ according to Eq. (A5) and lensing should in principle be identifiable for flux ratios $I \gtrsim 2\rho^{-2}$ and time delays $\Delta t_d \gtrsim f_{\rm cut}^{-1}$. We further showed in the right panel of Fig. 7 that the amplification factor of Eq. (15) is an excellent approximation to both the SIS and PM lens models in the geometrical-optics limit, suggesting that it should be suitable for model-independent searches for strong lensing in GW events.

The geometrical-optics approximation describes microlensing for lens masses in the range $M_{\rm min} \lesssim M_L \lesssim M_{\rm max}$, where

$$M_{\rm min} = (8\pi f)^{-1} = 400 M_\odot \left(\frac{f}{20\ {\rm Hz}}\right)^{-1}, \tag{21}$$

$$M_{\rm max} = 5(8\pi f)^{-8/3}\mathcal{M}^{-5/3} = 3\times 10^5 M_\odot \left(\frac{f}{20\ {\rm Hz}}\right)^{-8/3}\left(\frac{\mathcal{M}}{20 M_\odot}\right)^{-5/3}. \tag{22}$$

This complements electromagnetic observations of strong lensing which are only sensitive to lens masses $M_L \gtrsim 10^6 M_\odot$ [57–59]. GW lensing observations thus extend our sensitivity to isolated low-mass dark-matter halos by roughly three orders of magnitude. This is particularly important because cosmological observations challenge the ΛCDM model on these small scales [59,60]. This has motivated investigations of alternatives to cold dark matter which suppress the matter power spectrum or halo mass function on small scales.

Although gravitational lensing has not been detected in any of the GW events observed in the first three runs of the LVK detector network [14], recent estimates [61] suggest that $\sim 10^3$ strongly lensed GW events could be observed each year by future third-generation detectors like the proposed Cosmic Explorer (CE) [10] and Einstein Telescope (ET) [11]. The detection of gravitational lensing in GW events would be of tremendous scientific interest because it could test general relativity [28–30], probe the distribution of dark matter [62,63], and improve the precision of cosmological constraints [31] We propose that GW templates based on model-independent image parameters will be a valuable tool in this effort. In upcoming studies, we will investigate how effectively these GW templates can be used to identify additional images created by nonaxisymmetric lenses [64] and distinguish the effects of lensing from those of spin precession [65].

ACKNOWLEDGMENTS

This work is supported by National Science Foundation Grant No. PHY-2011977. The authors thank Christina McNally for discussions. The authors acknowledge the Texas Advanced Computing Center (TACC) at The University of Texas at Austin for providing HPC resources that have contributed to the research results reported within this paper [66].

APPENDIX A: MISMATCH IN THE EXTREME GEOMETRICAL-OPTICS LIMIT $\Delta t_d \to \infty$

We define the overlap $\mathcal{O}$ between a lensed waveform $\tilde{h}^L(f)$ and unlensed template $\tilde{h}(f)$ as

$$\mathcal{O} \equiv \frac{\langle \tilde{h}^L(f)|\tilde{h}(f)\rangle}{\sqrt{\langle \tilde{h}^L(f)|\tilde{h}^L(f)\rangle\langle \tilde{h}(f)|\tilde{h}(f)\rangle}}. \tag{A1}$$

For a lensed waveform with the amplification factor $F(f)$ of Eq. (15) appropriate for a two-image lens in the geometrical-optics approximation and an unlensed waveform with the same source parameters, this overlap becomes

$$\mathcal{O} = \frac{A_1}{\sqrt{A_2 A_3}}, \tag{A2}$$

where

$$A_1 \equiv \int df \frac{|\tilde{h}(f)|^2}{S_n(f)}(|\mu_+|^{1/2} + |\mu_-|^{1/2}\sin 2\pi f \Delta t_d), \tag{A3a}$$

$$A_2 \equiv \int df \frac{|\tilde{h}(f)|^2}{S_n(f)}(|\mu_+| + |\mu_-| + 2|\mu_+\mu_-|^{1/2}\sin 2\pi f \Delta t_d), \tag{A3b}$$

$$A_3 \equiv \int df \frac{|\tilde{h}(f)|^2}{S_n(f)}. \tag{A3c}$$

In the extreme geometrical-optics limit $\Delta t_d \to \infty$, the oscillatory terms do not contribute to the integrals implying $A_1 \to |\mu_+|^{1/2} A_3$, $A_2 \to (|\mu_+| + |\mu_-|)A_3$, and

$$\mathcal{O} \to \frac{|\mu_+|^{1/2}}{\sqrt{|\mu_+| + |\mu_-|}} = \frac{1}{\sqrt{1+I}} \tag{A4}$$

where $I = |\mu_-|/|\mu_+|$ is the flux ratio between the two images. Although the match 1-ϵ is normally calculated by maximizing the overlap over the coalescence time t_c and phase ϕ_c as in Eq. (19), it is independent of these parameters in the limit $\Delta t_d \to \infty$. This implies that the mismatch takes the limiting value

$$\epsilon \to 1 - \mathcal{O} = 1 - \frac{1}{\sqrt{1+I}}. \tag{A5}$$

APPENDIX B: INVESTIGATING OSCILLATIONS IN THE MISMATCH

In this Appendix, we examine the oscillations in the mismatch ϵ as a function of the time delay Δt_d seen in the bottom left panel of Fig. 8. We reproduce the $I = 0.2$ curve from this figure in Fig. 9 above. In the geometrical-optics approximation, lensing induces an oscillatory contribution to the GW phase that is poorly matched by a linear change to the GW phase resulting from a shift in the coalesence time t_c and phase ϕ_c according to Eq. (10). As such, the mismatch is well approximated as $\epsilon \approx 1 - \mathcal{O}$, where the overlap $\mathcal{O}$ is given by Eqs. (A1)–(A3). The crests and troughs of the oscillations in the mismatch as a function of the time delay Δt_d will therefore occur where

$$\frac{d\epsilon}{d\Delta t_d} = \mathcal{O}\left(\frac{1}{2A_2}\frac{dA_2}{d\Delta t_d} - \frac{1}{A_1}\frac{dA_1}{d\Delta t_d}\right) = \mathcal{O}\left(\frac{|\mu_+|^{1/2}}{A_2} - \frac{1}{A_1}\right)\frac{dA_1}{d\Delta t_d} \tag{B1}$$

vanishes.

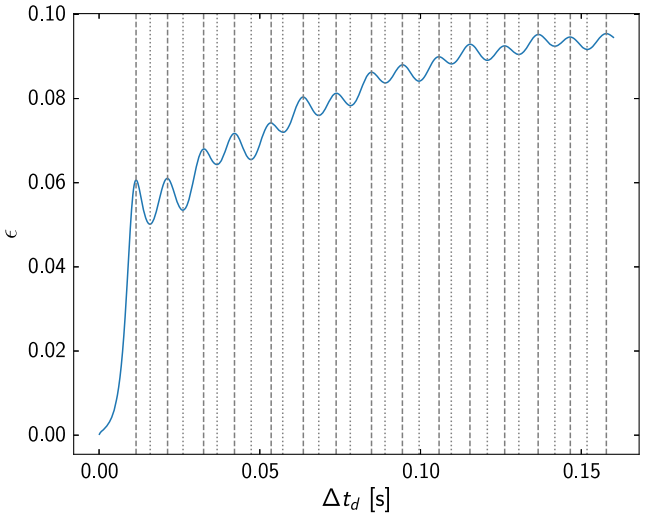

FIG. 9. The mismatch ϵ between a lensed GW source and unlensed templates for an SIS lens as a function of time delay Δt_d for flux ratio $I = 0.2$. The BBH system has source parameters $\mathcal{M} = 20M_\odot$, $\eta = 0.25$, and $t_c = \phi_c = 0$. The vertical dashed and dotted lines indicate the locations of the crests and troughs listed in Table I.

We show further that

$$\frac{dA_1}{d\Delta t_d} = |\mu_-|^{1/2} \int_{f_{\rm low}}^{f_{\rm cut}} df \frac{|\tilde{h}(f)|^2}{S_n(f)} 2\pi f \cos 2\pi f \Delta t_d \tag{B2a}$$

$$\approx \frac{|\mu_-|^{1/2}}{2\pi \Delta t_d^2} \left\langle \frac{|\tilde{h}(f)|^2}{S_n(f)} \right\rangle (w \sin w + \cos w)|_{w_{\rm low}}^{w_{\rm cut}} \tag{B2b}$$

$$\approx |\mu_-|^{1/2} \frac{A_3}{\Delta t_d} \sin w_{\rm cut}, \tag{B2c}$$

where we have defined $w \equiv 2\pi f \Delta t_d$, approximated $|\tilde{h}(f)|^2/S_n(f)$ by a constant in angular brackets equal to its average value, and assumed $w_{\rm cut} \gg w_{\rm low} \gg 1$ as will be true for small redshifted source masses in the geometrical-optics limit. Inserting these into Eq. (B1) and using the extreme geometrical-optics approximation described in Appendix A, we find

$$\frac{d\epsilon}{d\Delta t_d} = -\frac{I^{3/2}}{1+I} \frac{\mathcal{O}}{\Delta t_d} \sin w_{\rm cut}. \tag{B3}$$

This result implies that the crests [troughs] in the mismatch ϵ will occur at time delays $\Delta t_{d,c}$ [$\Delta t_{d,t}$] for which $w_{\rm cut} = 2n\pi$ [$(2n+1)\pi$], i.e.

TABLE I. The five columns in this table list: (1) the index n of the crests and troughs, (2) the numerically determined time delay of the crest, (3) the time delay of the crest predicted by Eq. (B4a), (4) the numerically determined time delay of the trough, and (5) the time delay of the trough predicted by Eq. (B4b). The lens and source parameters are the same as those in Fig. 9.

	Crests		Troughs	
n	Numerical Δt_d [ms]	Predicted $\Delta t_{d,c}$ [ms]	Numerical Δt_d [ms]	Predicted $\Delta t_{d,t}$ [ms]
1	11.51	10.47	15.91	15.71
2	21.31	20.94	26.12	26.18
3	32.52	31.41	36.72	36.65
4	42.13	41.88	47.33	47.12
5	53.53	52.36	57.13	57.59
6	63.54	62.83	68.34	68.06
7	73.75	73.30	78.15	78.53
8	84.75	83.77	88.95	89.01
9	94.36	94.24	99.56	99.48
10	105.8	104.7	109.6	109.9
11	115.4	115.2	120.8	120.4
12	126.2	125.7	130.6	130.9
13	136.6	136.1	141.8	141.4
14	146.6	146.6	151.8	151.8
15	157.8	157.1	⋯	⋯

$$\Delta t_{d,c} = n f_{\rm cut}^{-1} = n \times 10.47 \text{ ms} \left(\frac{M_z}{45.9 M_\odot} \right), \tag{B4a}$$

$$\Delta t_{d,t} = \left(n + \frac{1}{2} \right) f_{\rm cut}^{-1} = \left(n + \frac{1}{2} \right) 10.47 \text{ ms} \left(\frac{M_z}{45.9 M_\odot} \right). \tag{B4b}$$

Figure 9 reproduces the blue curve shown in the bottom left panel of Fig. 8 corresponding to the mismatch ϵ between a lensed GW source and unlensed templates in the SIS model for flux ratio $I = 0.2$ and source parameters $\mathcal{M} = 20M_\odot$, $\eta = 0.25$, and $t_c = \phi_c = 0$. The dashed (dotted) vertical lines indicate the values of the time delay at which maxima (minima) of the mismatch occur. These numerically determined values are listed in Table I, where they are compared to the values predicted by Eqs. (B4a) and (B4b). We see that there is excellent agreement between our numerical results and analytical predictions, and that this agreement improves for larger times delays Δt_d at which the extreme geometrical-optics approximation becomes increasingly valid.

[1] B. Abbott, R. Abbott, T. Abbott, M. Abernathy, F. Acernese, K. Ackley, C. Adams, T. Adams, P. Addesso, R. Adhikari *et al.*, Phys. Rev. Lett. **116**, 061102 (2016).
[2] J. Aasi *et al.* (LIGO Scientific Collaboration), Classical Quantum Gravity **32**, 074001 (2015).
[3] F. Acernese *et al.* (Virgo Collaboration), Classical Quantum Gravity **32**, 024001 (2015).
[4] R. Abbott, T. Abbott, F. Acernese, K. Ackley, C. Adams, N. Adhikari, R. Adhikari, V. Adya, C. Affeldt, D. Agarwal *et al.*, arXiv:2111.03606.
[5] K. Somiya (KAGRA Collaboration), Classical Quantum Gravity **29**, 124007 (2012).
[6] Y. Aso, Y. Michimura, K. Somiya, M. Ando, O. Miyakawa, T. Sekiguchi, D. Tatsumi, and H. Yamamoto (The KAGRA Collaboration), Phys. Rev. D **88**, 043007 (2013).
[7] T. Akutsu *et al.* (KAGRA Collaboration), Prog. Theor. Exp. Phys. **2021**, 05A101 (2021).
[8] R. Abbott, H. Abe, F. Acernese, K. Ackley, N. Adhikari, R. Adhikari, V. Adkins, V. Adya, C. Affeldt, D. Agarwal *et al.*, arXiv:2112.06861 [Phys. Rev. D (to be published)].
[9] LIGO Scientific, Virgo, KAGRA Collaborations, arXiv: 2111.03604.
[10] M. Evans, R. X. Adhikari, C. Afle, S. W. Ballmer, S. Biscoveanu, S. Borhanian, D. A. Brown, Y. Chen, R. Eisenstein, A. Gruson *et al.*, arXiv:2109.09882.
[11] M. Maggiore *et al.*, J. Cosmol. Astropart. Phys. 03 (2020) 050.
[12] S. Kawamura *et al.*, Prog. Theor. Exp. Phys. **2021**, 05A105 (2021).
[13] E. Barausse *et al.*, Gen. Relativ. Gravit. **52**, 81 (2020).
[14] R. Abbott, T. D. Abbott, S. Abraham, F. Acernese, K. Ackley, A. Adams, C. Adams, R. X. Adhikari (LIGO Scientific, and Virgo Collaborations), Astrophys. J. **923**, 14 (2021).
[15] J. K. Lawrence, Nuovo Cimento B Serie **6B**, 225 (1971).
[16] H. C. Ohanian, Int. J. Theor. Phys. **9**, 425 (1974).
[17] T. T. Nakamura and S. Deguchi, Prog. Theor. Phys. Suppl. **133**, 137 (1999).
[18] T. T. Nakamura, Phys. Rev. Lett. **80**, 1138 (1998).
[19] R. Takahashi and T. Nakamura, Astrophys. J. **595**, 1039 (2003).
[20] M. Oguri, Mon. Not. R. Astron. Soc. **480**, 3842 (2018).
[21] S.-S. Li, S. Mao, Y. Zhao, and Y. Lu, Mon. Not. R. Astron. Soc. **476**, 2220 (2018).
[22] J. M. Ezquiaga, D. E. Holz, W. Hu, M. Lagos, and R. M. Wald, Phys. Rev. D **103**, 064047 (2021).
[23] P. Schneider, Astron. Astrophys. **143**, 413 (1985).
[24] P. Schneider, J. Ehlers, and E. E. Falco, *Gravitational Lenses* (Springer, 1999).
[25] K.-H. Lai, O. A. Hannuksela, A. Herrera-Martín, J. M. Diego, T. Broadhurst, and T. G. F. Li, Phys. Rev. D **98**, 083005 (2018).
[26] J. M. Diego, Phys. Rev. D **101**, 123512 (2020).
[27] M. Oguri and R. Takahashi, Astrophys. J. **901**, 58 (2020).
[28] T. Baker and M. Trodden, Phys. Rev. D **95**, 063512 (2017).
[29] T. E. Collett and D. Bacon, Phys. Rev. Lett. **118**, 091101 (2017).
[30] S. Mukherjee, B. D. Wandelt, and J. Silk, Mon. Not. R. Astron. Soc. **494**, 1956 (2020).
[31] S. Goyal, K. Haris, A. K. Mehta, and P. Ajith, Phys. Rev. D **103**, 024038 (2021).
[32] O. A. Hannuksela, T. E. Collett, M. Çalışkan, and T. G. F. Li, Mon. Not. R. Astron. Soc. **498**, 3395 (2020).
[33] M. Sereno, P. Jetzer, A. Sesana, and M. Volonteri, Mon. Not. R. Astron. Soc. **415**, 2773 (2011).
[34] K. Liao, X.-L. Fan, X.-H. Ding, M. Biesiada, and Z.-H. Zhu, Nat. Commun. **8**, 1148 (2017); **8**, 2136(E) (2017).
[35] S. Cao, J. Qi, Z. Cao, M. Biesiada, J. Li, Y. Pan, and Z.-H. Zhu, Sci. Rep. **9**, 11608 (2019).
[36] Y. Li, X. Fan, and L. Gou, Astrophys. J. **873**, 37 (2019).
[37] H. Yu, P. Zhang, and F.-Y. Wang, Mon. Not. R. Astron. Soc. **497**, 204 (2020).
[38] E. Wempe, L. V. Koopmans, A. Wierda, O. A. Hannuksela, and C. v. d. Broeck, arXiv:2204.08732.
[39] C. Cutler and E. E. Flanagan, Phys. Rev. D **49**, 2658 (1994).
[40] J. Janquart, O. A. Hannuksela, K. Haris, and C. Van Den Broeck, Mon. Not. R. Astron. Soc. **506**, 5430 (2021).
[41] R. K. L. Lo and I. Magana Hernandez, arXiv:2104.09339.
[42] A. More and S. More, Mon. Not. R. Astron. Soc. **515**, 1044 (2022).
[43] M. Wright and M. Hendry, Astrophys. J. **935**, 68 (2022).
[44] K. Subramanian and S. A. Cowling, Mon. Not. R. Astron. Soc. **219**, 333 (1986).
[45] R. Takahashi, Astron. Astrophys. **423**, 787 (2004).
[46] T. A. Apostolatos, C. Cutler, G. J. Sussman, and K. S. Thorne, Phys. Rev. D **49**, 6274 (1994).
[47] R. Gavazzi, T. Treu, J. D. Rhodes, L. V. E. Koopmans, A. S. Bolton, S. Burles, R. J. Massey, and L. A. Moustakas, Astrophys. J. **667**, 176 (2007).
[48] N. Matsunaga and K. Yamamoto, J. Cosmol. Astropart. Phys. 01 (2006) 023.
[49] P. C. Peters, Phys. Rev. D **9**, 2207 (1974).
[50] R. J. Bontz and M. Haugan, Astrophys. Space Sci. **78**, 199 (1981).
[51] A. Nitz *et al.*, gwastro/pycbc: v2.0.2 release of pycbc (2022).
[52] L. S. Finn, Phys. Rev. D **46**, 5236 (1992).
[53] L. S. Finn and D. F. Chernoff, Phys. Rev. D **47**, 2198 (1993).
[54] A. H. Mroue *et al.*, Phys. Rev. Lett. **111**, 241104 (2013).
[55] J. Aasi *et al.* (LIGO Scientific, Virgo, NINJA-2 Collaborations), Classical Quantum Gravity **31**, 115004 (2014).
[56] M. Boyle *et al.*, Classical Quantum Gravity **36**, 195006 (2019).
[57] S. Mao and P. Schneider, Mon. Not. R. Astron. Soc. **295**, 587 (1998).
[58] N. Dalal and C. S. Kochanek, Astrophys. J. **572**, 25 (2002).
[59] D. Gilman, S. Birrer, A. Nierenberg, T. Treu, X. Du, and A. Benson, Mon. Not. R. Astron. Soc. **491**, 6077 (2020).
[60] J. S. Bullock and M. Boylan-Kolchin, Annu. Rev. Astron. Astrophys. **55**, 343 (2017).
[61] M. Oguri, Mon. Not. R. Astron. Soc. **480**, 3842 (2018).
[62] X. Guo and Y. Lu, Phys. Rev. D **106**, 023018 (2022).
[63] S. Cao, J. Qi, Z. Cao, M. Biesiada, W. Cheng, and Z.-H. Zhu, Astron. Astrophys. **659**, L5 (2022).

[64] S. Ali, E. Stoikos, M. Kesden, and L. King, Identifying multiple images of gravitational-wave sources lensed by elliptical lensing potentials (2023), to be published.

[65] E. Stoikos, S. Ali, M. Kesden, and L. King, Distinguishing the effects of spin precession and gravitational lensing in gravitational-wave observations of binary black-hole mergers (2023), to be published.

[66] D. Stanzione, B. Barth, N. Gaffney, K. Gaither, C. Hempel, T. Minyard, S. Mehringer, E. Wernert, H. Tufo, D. Panda, and P. Teller, in *Proceedings of the Practice and Experience in Advanced Research Computing 2017 on Sustainability, Success and Impact, PEARC17* (Association for Computing Machinery, New York, NY, USA, 2017).